

Measurements of the energy distribution of an ultracold rubidium ion beam

G. ten Haaf, S.H.W. Wouters, D.F.J. Nijhof, P.H.A. Mutsaers, and E.J.D. Vredenburg*

Department of Applied Physics, Eindhoven University of Technology,

P.O. Box 513, 5600 MB Eindhoven, the Netherlands

(Dated: July 2, 2021)

The energy distribution of an ultracold rubidium ion beam, which is intended to be used as the source for a focused ion beam instrument, is measured with a retarding field analyzer. The ions are created from a laser-cooled and compressed atomic beam by two-step photoionization in which the ionization laser power is enhanced in a build-up cavity. Particle tracing simulations are performed to ensure the analyzer is able to resolve the distribution. The lowest achieved full width 50% energy spread is (0.205 ± 0.006) eV. The energy spread originates from the variation in the ionization position of the ions which are created inside an extraction electric field. This extraction field is essential to limit disorder-induced heating which can decrease the ion beam brightness. The ionization position distribution is limited by a tightly focused excitation laser beam. Energy distributions are measured for various ionization and excitation laser intensities and compared with calculations based on numerical solutions of the optical Bloch equations including ionization. A good agreement is found between measurements and calculations.

I. INTRODUCTION

The ability to modify substrates at the nanometer length scale makes focused ion beams (FIBs) indispensable tools in the semiconductor industry and nanofabrication research. Important applications are transmission electron microscope (TEM) sample preparation [1], failure analysis [2] and circuit edit [3]. The current industry standard source for FIBs for these nanofabrication purposes is the liquid metal ion source (LMIS). A LMIS-based FIB reaches a resolution of 5-10 nm with a 1 pA beam of 30 keV ions. Due to chromatic aberrations of the electrostatic lens system this probe size is for a large part limited by the 4.5 eV (FWHM) LMIS energy spread [4]. Since chromatic aberrations scale with the relative energy spread, this limitation becomes even more important when a low energy beam is required, for example to lower the ion penetration depth and prevent nanopore formation or amorphization of crystalline samples [5].

Ultracold ion sources [6] are promising candidates to replace the LMIS in FIBs for nanofabrication purposes. Recently, for example, a resolution of 2.8 nm (25%-75% rise distance, 1.2 pA, 10 keV) was demonstrated with a focused ion beam equipped with an ultracold cesium ion source [7]. These ultracold sources are based on the ionization of laser cooled atoms. The low transverse temperature of the atoms enable ion beam brightnesses of the order of 10^7 A/m²/sr/eV and energy spreads are expected to be smaller than 1 eV [8–10]. Here, direct measurements of the energy distribution of an ultracold Rb ion beam are presented. These show that the energy spread can be as low as 0.2 eV and independent of ion beam energy.

The ultracold Rb ion beam is formed in the atomic beam laser cooled ion source (ABLIS). In this source

an ultracold beam of ⁸⁵Rb atoms is created by means of magneto-optical compression [11]. After selection of the desired atomic flux, this beam is photoionized in the crossover of a tightly focused excitation laser beam and an ionization laser beam whose intensity is enhanced in a build-up cavity [12]. The ions are immediately extracted by an electric field in order to prevent disorder-induced heating which can lower the ion beam brightness [13]. The energy spread in the beam mostly originates from the distribution in the ionization position within this extraction field. Here, a retarding field analyzer [14] is used to measure the energy distribution. A comparison with expected ionization position distributions [12] is presented for various experimental parameters.

The remainder of this manuscript is organized as follows. Section II first presents details of the experimental setup creating the ultracold Rb ion beam and then introduces the retarding field analyzer that was constructed to measure the energy distribution. Particle tracing simulations, which are performed to analyze how the finite resolution of the retarding field analyzer affects the measurement, are presented in section III. Section IV first introduces some methods used to optimize the outcome of the experiments and then shows energy distribution measurements for different extraction fields, laser intensities, beam current and beam energy. The conclusions are summarized in section V.

II. EXPERIMENTAL SETUP

The ion beam analyzed in this research is created by two-step photoionization of a laser-cooled and compressed beam of ⁸⁵Rb atoms. The details of the creation and analysis of this atomic beam were described earlier [11]. There, also a measurement of the longitudinal velocity distribution of the atoms is shown. From these laser-induced fluorescence results, the full width 50% energy spread of the incoming atoms is determined to be

* e.j.d.vredenburg@tue.nl

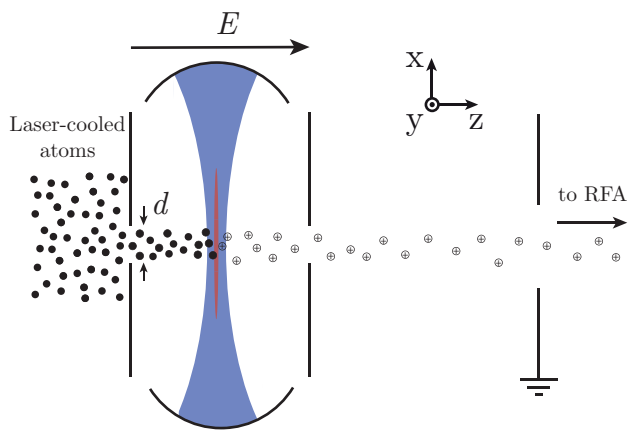


FIG. 1. Schematic picture of the photoionization and acceleration setup in the ABLIS setup. The atomic beam is skimmed with a selection aperture to only let through the ions which are desired to be ionized. The ionization takes place at the crossover of a tightly focused excitation laser beam and an ionization laser beam whose intensity is enhanced in a build-up cavity. This crossover is positioned in the first of two acceleration stages in which an extraction electric field E is present. Acceleration takes place in two steps in order to set the extraction field separately from the final beam energy.

4 meV. As will be shown this is much smaller than the energy spread caused by the variation in ionization position.

The photoionization and acceleration setup is schematically depicted in figure 1. After laser cooling and compression the atomic beam is skimmed by an aperture with diameter d on a movable aperture strip. Photoionization takes place in the crossover of a tightly cylindrically focused excitation laser beam and an ionization laser beam whose intensity is enhanced in a build-up cavity. More details of the ionization setup are given in Ref. [12]. Calculations also discussed in this reference show that for high ionization laser beam intensities the ionization region can be limited in the z -direction by solely focusing the excitation laser beam very tightly. The $1/e^2$ diameters of the ionization and excitation laser beams are estimated at $68 \mu\text{m}$ and $16 \mu\text{m}$ respectively.

Particle tracing simulations that were performed earlier [13] showed that a reduction of the ion beam brightness due to disorder-induced heating can be prevented by applying an extraction electric field with such a magnitude that a so-called pencil beam is created. The extraction field needed to reach the pencil beam regime increases with the beam current since a larger beam current is made by increasing the size of the selection aperture. Since the ion beam energy spread is also determined by this field, it will be beneficial to change the extraction field when the beam current is changed in a future FIB instrument. To enable setting this extraction field E separately from the total beam energy U , the ABLIS accelerator consists of two acceleration sections. The ionization takes place between two electrodes that

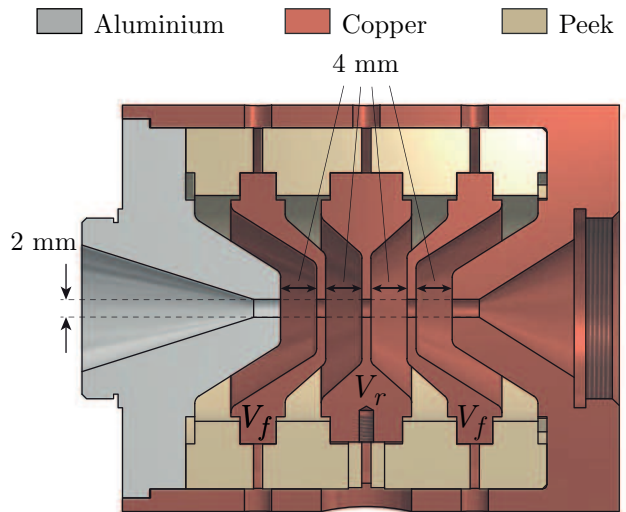


FIG. 2. Cross section of the retarding field analyzer (RFA) that is used to measure the energy distribution. The ion beam enters the RFA from the left. The legend indicates what materials the colors correspond to. The three middle electrodes are all electrically isolated from the rest. The middle electrode is set at a potential V_r , so that only ions with an energy $U > eV_r$ are transmitted. The second and fourth electrode are set at a potential V_f , which is varied in particle tracing simulations in order to maximize the energy resolution. The first electrode and the surrounding fifth electrode are grounded. The Faraday cup used to measure the transmitted current is placed directly after the RFA, but is not shown in the image. Screw thread on the outside of the extrusion on the left is used to connect the RFA to the last electrode of the accelerator.

near the axis can be approximated by flat plates with an aperture in them. Near the axis, the separation between the electrodes is 3 mm and the diameter of the aperture in the second electrode through which the ions are extracted is 2 mm. Further from the axis, the electrodes are separated more to make room for the lens that focuses the excitation beam. The third electrode is a flat plate with an aperture with a diameter of 7 mm.

Due to the changing electric fields, the acceleration structure causes a lens action on the ion beam, which deflects ions that are travelling off-axis. This deflection is unwanted as it can decrease the ion beam brightness and, as will be discussed later, decrease the energy resolution of the retarding field analyzer. Therefore, the ions need to be created on the axis of the accelerator. To facilitate alignment, the whole accelerator structure is placed on a flexure hinge that enables planar movement in the transverse directions. The position of the accelerator can be adjusted with an accuracy of $22 \mu\text{m}$ with two micrometer feedthroughs.

In a retarding field analyzer the incoming ions are decelerated by a retarding potential V_r . If this potential exceeds the energy of an incoming ion, the ion is reflected. Otherwise the ion is collected by some measurement device or reaccelerated and collected at a later stage. By

varying V_r and measuring the collected or transmitted current, the energy distribution of the ions is determined. A cross section of the RFA used here is shown in figure 2. It is similar to the intermediate image lens arrangement described by Simpson [14]. In such an analyzer the ions are decelerated in two stages, giving rise to a lens action with which the ions can be focused on the center electrode. The top of the potential barrier is positioned in free space within the aperture of this center electrode. After the retarding electrode the ions are accelerated again to their original energy and collected by a Faraday cup (not shown in figure 2). The apertures in all five electrodes have a 2 mm diameter. The middle three electrodes are 1 mm thick in the center. The second and fourth electrode are set at an electric potential V_f . The RFA is connected to the last accelerator electrode by means of a screw thread on the outside of the extrusion on the left side in figure 2. This means that the RFA moves simultaneously with the accelerator when it is translated.

III. RETARDING FIELD ANALYZER ENERGY RESOLUTION

There are two aspects that determine the resolution of the retarding field analyzer. The first one is the variation of the height of the potential barrier over the position within the aperture in combination with the size of the beam. The other one is the direction of the local field in combination with the angular spread with which the ion beam approaches the potential barrier. Both, the size of the beam as well as its angular spread are influenced by the potential on the focusing electrode. In this section the optimal V_f , that gives the highest energy resolution, is determined using General Particle Tracer (GPT) simulations [15].

In the GPT simulation, the ions are initialized inside the accelerator and their equations of motion are solved while taking into account the electric field of the accelerator and the RFA. These fields are interpolated on a cylindrically symmetric electric field map calculated with CST EM-studio [16]. Also the geometries are taken into account, i.e., an ion that does not go through an aperture is removed from the simulation. In this way an RFA measurement can be simulated by determining the fraction of ions that is transmitted through all apertures as a function of V_r . The full width 50% apparent energy spread, i.e., including finite resolution effects, is extracted from the simulation. The transverse position and velocity distribution are initialized according to the previously introduced Monte Carlo procedure which takes into account the effect of the selection aperture [12]. Similar as in most experiments, the diameter of the selection aperture was $21 \mu\text{m}$. The longitudinal position distribution, giving rise to the energy spread, is calculated from a numerical solution to the optical Bloch equations including ionization [12]. This distribution with a full width 50%

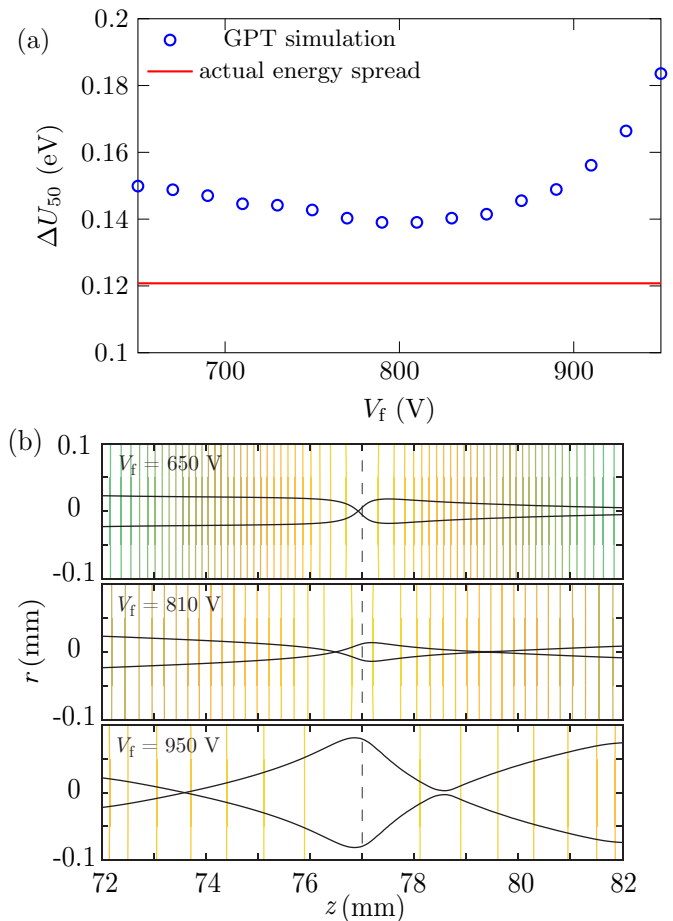


FIG. 3. Particle tracing simulation results of energy spread measurements using the retarding field analyzer. (a) Apparent energy spread of the ion beam, i.e., including finite resolution effects (markers) as a function of the focusing voltage V_f . The line indicates the actual energy spread, directly calculated from the ion velocities. (b) Beam envelopes containing 50% of the beam current as a function of the longitudinal position z for three different values of the focusing voltage. The retarding electrode is positioned at $z = 77$ mm and the focusing electrode is positioned at $z = 72$ mm. These positions are relative with respect to the position of ionization. The simulation were performed for: $U = 1$ keV, $E = 37$ kV/m and $d = 21 \mu\text{m}$.

position spread of $3.3 \mu\text{m}$ is calculated for an ionization laser intensity of $1.7 \times 10^{10} \text{ W/m}^2$ and an excitation laser saturation parameter of 1.3×10^2 . These values are chosen since they resulted in the lowest energy spread in the experiment, as will be shown in section IV.

The results of the simulations are summarized in figure 3. In these simulations the ions are extracted with an extraction field of 37 kV/m and the beam energy was 1 keV . Figure 3a shows the full width 50% energy spread ΔU_{50} as a function of V_f . The markers show the apparent energy spread obtained using the RFA, while the line indicates the actual energy spread directly calculated from the incoming ion velocities. The highest resolution is ob-

tained around $V_f \approx 800$ V, where the overestimation of the energy spread is only 20 meV. Between $V_f = 750$ V and $V_f = 850$ V the resolution is good and relatively insensitive for changes V_f . The trend of the RFA resolution can be understood from the beam envelopes plotted in figure 3b for three different V_f . For $V_f = 650$ V the beam is focused almost exactly at the center of the retarding electrode which is indicated by the dashed line. Therefore the analysis suffers very little from a difference in height of the potential barrier. However, the ions travel towards the center of the aperture, while the local field is also pointing from the rim of the aperture to its center. A higher resolution is reached when the beam is slightly divergent when it travels towards the potential barrier, since the ion trajectories are then better aligned in the direction opposing the local field. This situation is reached for $V_f = 810$ V as can be seen in the second plot of figure 3b. When V_f is increased further the resolution decreases again because the beam probes a larger region of the retarding electrode aperture, as be seen in the last plot.

The GPT simulations show that the energy distribution is slightly broadened due to the finite resolution of the RFA. In the case of a 1 keV beam, the apparent energy spread is only one sixth higher than the expected energy spread of the ions. However, note that in the simulation a perfect alignment is assumed, i.e., the beam is perfectly aligned with the RFA axis and the electrodes are also perfectly coaxial. Misalignment decreases the RFA resolution. This is further discussed in subsection IV E. Furthermore, the smallest resolvable energy spread scales with the beam energy since the potential drop from the rim of the retarding electrode aperture to the axis becomes larger. This is discussed in subsection IV G.

IV. MEASUREMENTS

In this section the performed energy distribution measurements are presented. Subsections IV A and IV B introduce the methods to align the beam and average the results. Subsections IV E-IV G discuss the energy distributions obtained for different experimental settings.

A. Alignment

The ions should be created on the axis of the system to obtain the highest energy resolution with the retarding field analyzer. In order to do so, the current is measured as a function of the accelerator position. In these measurements there was no voltage applied to any of the RFA electrodes which were only used to cut off the beam when it is deflected too far from the axis. The result of three of such measurements at different extraction field strengths is shown in figure 4. The markers show the measured current as a function of the initial position x_0 of the ion beam with respect to the accelerator axis. The

centers of the three flat top profiles indicate the position at which the position of ionization is exactly on the axis.

Interestingly the flat top profile first increases in width for an increasing extraction field and then decreases. This can be explained by looking at particle tracing simulation results which are also plotted in figure 4a and show the same behaviour. Figure 4b shows the average trajectories of the ions in these simulations for several different x_0 and for the three different extraction fields. The figure also shows the equipotential lines of the accelerator and the contours of the RFA electrodes. From these ion beam trajectories the changes in the width of the profiles in figure 4a can be understood. Due to the curvature of the electric field at the end of the extraction region the ions experience an exit kick that diverges the ion beam, but in this case more important, also bends the whole beam outwards when it is created off-axis. In the second acceleration stage the deflected ions then first experience a force directed to the axis in the increasing field section and then again a force directed from the axis in the decreasing field section. As can be seen, this causes the beam to go through a crossover at low extraction fields. The overall effect of an increase in extraction field and corresponding decrease in post-acceleration field is that the position of this crossover is displaced to larger z , i.e., the beam leaves the accelerator less converging. From the trajectories in figure 4b it can be concluded that when the crossover is inside the RFA the profile in 4a is the widest because the displacement from the axis at the position of the RFA electrodes is then smallest for a given x_0 .

B. Averaging method

Most of the experimental energy distributions shown in this manuscript are measured by averaging 15 curves of the current I as a function of the retarding voltage V_r . Figure 5a shows a typical example of these 15 unaveraged curves. Measuring a single curve takes approximately two and a half minutes. As can be seen the curves are all very similar apart from noise, small energy drifts and amplitude drifts. To reduce the noise, especially in the numerical derivatives, the curves are averaged. However, note that the individual curves are all slightly shifted with respect to each other, i.e., there is a drift in the beam energy. The reason for this shift is not known, but a possible explanation could be charging of dielectric surfaces near the accelerator structure. As this drift takes place over a rather large timescale it is not considered an energy spread. Therefore it is corrected for by shifting the individual curves with the voltage at which half of the maximum current is reached. This value was found from a linear fit through the data points between 25% and 75% of the maximum current. Furthermore, the curves are divided by the maximum current I_{\max} , so that the derivative of the curve results in a normalized energy distribution. The resulting averaged shifted nor-

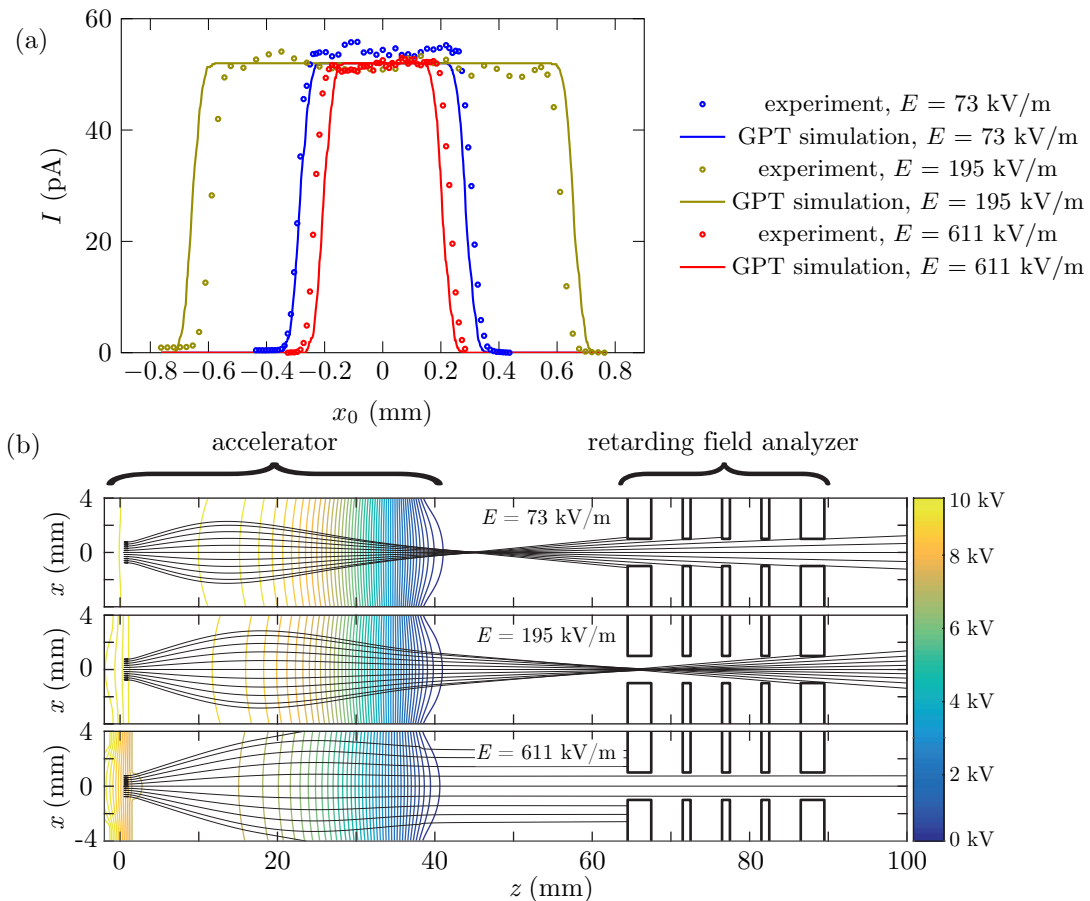


FIG. 4. (a) Experimental data (markers) and simulation data (lines) of the beam current transmitted through the apertures in the retarding field analyzer electrodes as a function of the center transverse position x_0 at which the ions are created. The measurement was performed with the three values of the extraction field E indicated in the legend. (b) Equipotential map of the accelerator for the three extraction fields in (a) and the average ion beam trajectories (black lines) for 11 different x_0 . The thick black lines indicate the contours retarding field analyzer electrodes.

malized curves are shown in the top panel of figure 5b. The derivative of this curve results in the normalized energy distribution and is shown in the bottom panel of figure 5b. The error bars indicate the standard deviation of the mean value.

In the next sections, results are shown of systematic variations of experimental parameters, such as the ionization intensity I_i , the excitation saturation parameter s and the acceleration field. In order to quantitatively compare these experimental results with each other a full width 50% energy spread ΔU_{50} is determined from the energy distributions. This value is the smallest width of the distribution that contains 50% of the normalized current. For the data shown in figure 5b, this resulted in $\Delta U_{50} = (0.290 \pm 0.009)$ eV, in which the uncertainty indicates the 68% confidence interval.

C. Ionization laser beam intensity

The longitudinal extent of the ionization region in the ABLIS setup (see figure 1), and thus also the energy spread of the resulting ion beam, is limited by the size of the excitation laser beam. However, the exact distribution is also influenced by the ionization laser beam intensity I_i . Here the effect of I_i on the ion energy distribution is determined experimentally. Since the ion energy is directly proportional to the extraction field, the ionization position z can be calculated by the transformation,

$$z = -\frac{V_r}{E} + \zeta \quad (1)$$

in which ζ is a constant determined by the absolute ionization position. With this transformation the ion energy distribution can be transformed in the ionization position distribution. This allows for comparison with solutions of the optical Bloch equations including ionization. Figure 6a shows the measured ionization position distributions for four different values of I_i together with calculated dis-

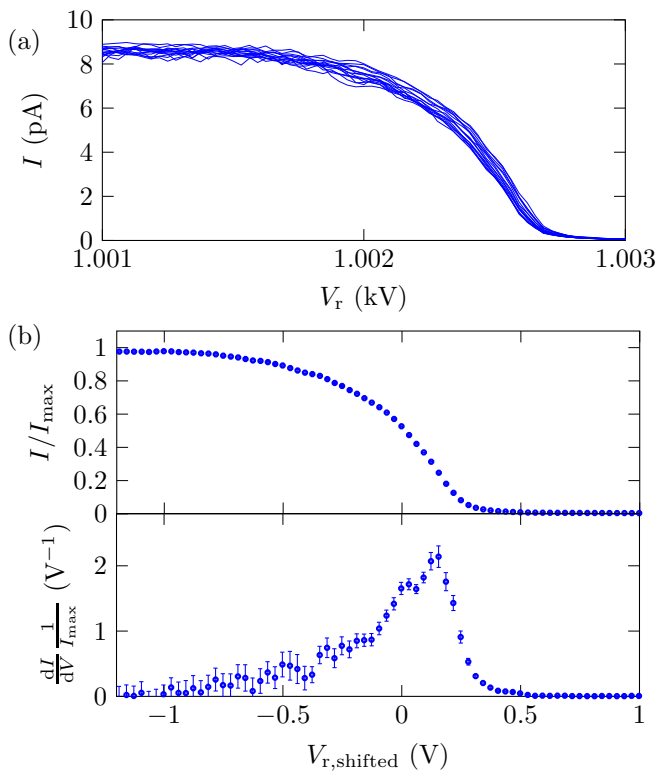


FIG. 5. (a) Measured current as function of the retarding voltage ($15\times$). (b) The averaged shifted normalized current of the curves from (a) (top panel) and its derivative (bottom panel) as a function of the shifted retarding voltage. The data is measured with $I_i = 2 \times 10^9 \text{ W/m}^2$, $s = 1.3 \times 10^2$, $U = 1 \text{ keV}$, $E = 37 \text{ kV/m}$, $V_f = 850 \text{ V}$ and $d = 21 \text{ }\mu\text{m}$.

tributions. The constant ζ is determined by a fit of the measured distribution with the calculated one for each distribution separately. The position $z = 0$ corresponds to the center of the laser beams as can be seen in the top panel.

The resemblance between the measurement and calculation is remarkable. The measured data reproduces the shape of the distribution very well. At the negative z -side, corresponding to the highest energies, there is a sharp rise in the distribution due to the onset of excitation. The tail on the positive z -side gets smaller for increasing I_i . In the distribution for $I_i = 2.7 \times 10^8 \text{ W/m}^2$ ionization stops because the atoms have returned to the ground state. For $I_i = 9.7 \times 10^9 \text{ W/m}^2$ the ionization is quenched since most of the atoms are ionized. Figure 6b shows the resulting energy spread as a function of I_i . The trend of the measured energy spread and its calculated counterpart is similar. However, at low I_i the calculation predicts a somewhat lower energy spread. A possible explanation for this difference can be an experimental excitation laser beam shape not fully resembling the one in the calculation. The smallest measured energy spread is $(0.205 \pm 0.006) \text{ eV}$, corresponding to a full width 50% ionization position distribution width of $(5.6 \pm 0.2) \text{ }\mu\text{m}$.

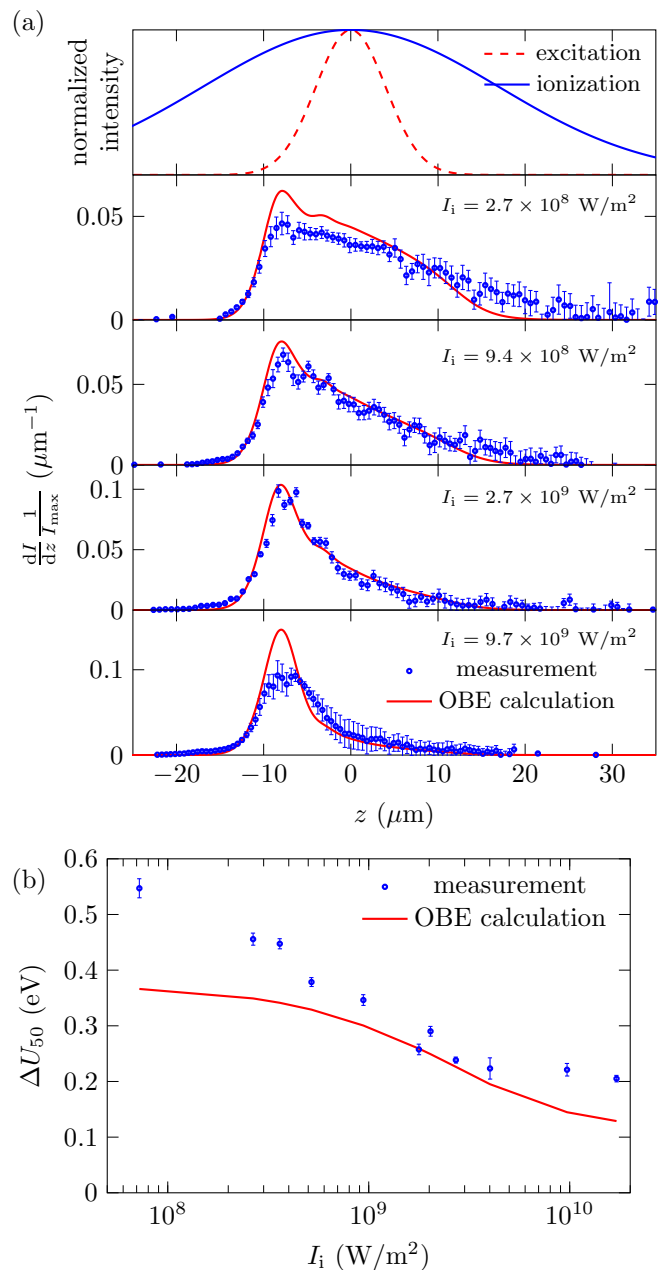


FIG. 6. (a) Measured (markers with error bars indicating the standard deviation) and calculated (lines) ionization position distributions for four different values of the ionization laser beam intensity (bottom four panels). The top panel shows the shape of excitation and ionization laser beams that are used in the calculation. (b) Measured (markers with error bars indicating the standard deviation) and calculated (lines) full width 50% energy spread as a function of the ionization laser beam intensity. Experiments are performed with $s = 1.3 \times 10^2$, $E = 37 \text{ kV/m}$, $U = 1 \text{ keV}$, $V_f = 850 \text{ V}$ and $d = 21 \text{ }\mu\text{m}$.

D. Excitation laser beam intensity

The ion energy distribution is also measured for varying excitation laser beam intensity I_e , expressed in terms

of the saturation parameter $s = \frac{I_e}{I_s}$. The values of s are determined at the center of the excitation beam and are calculated with a saturation intensity $I_s = 51 \text{ W/m}^2$ [12]. The results are shown in figure 7, which again shows four ionization position distributions and a plot of the ΔU_{50} as a function of s . The results are measured and calculated for the highest I_i in figure 6.

For $s = 27$ and $s = 1.3 \times 10^2$ there is a reasonable agreement between the measured and calculated distribution. As can be seen in figure 7b the widths of the distributions also agrees best in this region. Furthermore, the trend of a decreasing distribution width is also as expected at low s . However, for $s > 200$ the width increases again. The reason for this is most likely that the excitation laser beam shape did not fully resemble a Gaussian far from its center on the negative z -side. On the positive z -side, the laser beam shape did probably not resemble a Gaussian at all since the measured distribution for $s = 2.4$ is much wider on this side. For higher s this does not result in longer tails on the positive z -side because most of the atoms are already ionized before reaching it. A cause for such an excitation beam shape can be that it did not go through the focusing lens in its center, which due to interference and aberrations can lead to an asymmetric shape in the beam waist. All other measurements shown in this manuscript are measured with $s = 1.3 \times 10^2$.

E. Extraction field strength

As was explained in section I the energy spread is expected to be proportional to the extraction field. A measurement was performed to test this expectation. The results are shown in figure 8, which shows the measured energy spread (markers with error bars) as a function of the extraction field. Without looking at the other lines in the figure yet the energy spread indeed seems to grow linearly with the extraction field. However, when taking a closer look the energy spread increases slightly faster. This is especially visible when comparing the measurement with the expected relation that is also plotted (solid line). This relation is calculated by multiplication of the ionization position distribution width, found by solving the optical Bloch equations including ionization [12], with the applied extraction field. At low extraction field strengths the energy spread is somewhat higher than expected, but it does increase with the expected slope. There are some fluctuations that are clearly larger than the error margin. These could be caused by a dependence of the ionization cross section on the electric field [17, 18]. The deviations between expectation and measurement are more prominent at increased extraction field strengths.

A possible explanation for the deviation between the expected trend and the measurement are misalignments between the ionization position, the accelerator electrodes and the RFA electrodes. The effect of misalignments is investigated using similar particle tracing simulations as in section 3. Figure 8 shows the particle tracing

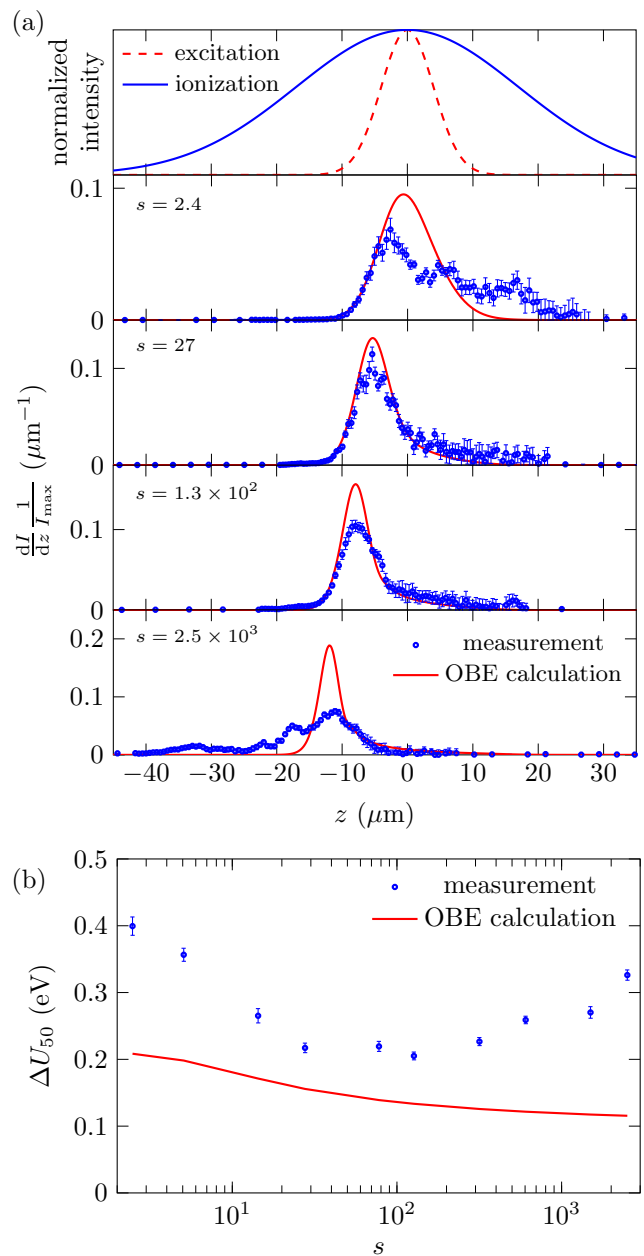


FIG. 7. (a) Measured (markers with error bars indicating the standard deviation) and calculated (lines) ionization position distributions for four different values of the excitation laser beam saturation parameter (bottom four panels). The top panel shows the shape of excitation and ionization laser beams that are used in the calculation. (b) Measured (markers with error bars indicating the standard deviation) and calculated (lines) full width 50% energy spread as a function of the excitation laser beam saturation parameter. Experiments are performed with $I_i = 1.7 \times 10^{10} \text{ W/m}^2$, $E = 37 \text{ kV/m}$, $U = 1 \text{ keV}$, $V_i = 850 \text{ V}$ and $d = 21 \text{ } \mu\text{m}$.

results for three different cases: one in which the ions are created exactly on the axis, one where the ions are created at an offset of $22 \text{ } \mu\text{m}$ and one in which this offset was $44 \text{ } \mu\text{m}$. The simulations show that the trend indeed

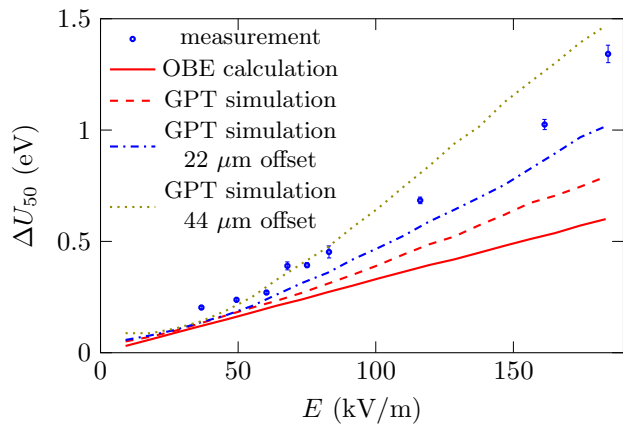


FIG. 8. Full width 50% energy spread as a function of the extraction field. The markers show the experimentally determined energy spread and the error bars the standard deviation on this value. The solid line shows the expected linear relation between ΔU_{50} and E . The slope of this line is the spread in the ionization position which is found from a solution of the optical Bloch equations including ionization. The three dashed/dotted lines show the results of particle tracing simulations in which the experiment was simulated for three cases: ions created on the axis of the system, ions created at $22 \mu\text{m}$ from the axis and ions created at $44 \mu\text{m}$ from the axis. The experimental results shown are measured with $I_i = 1.7 \times 10^{10} \text{ W/m}^2$, $s = 1.3 \times 10^2$, $U = 1 \text{ keV}$, $V_f = 850 \text{ V}$ and $d = 21 \mu\text{m}$.

becomes more non-linear for larger misalignments. The reason for this behaviour is that when the extraction field is increased the ions leave the accelerator under a larger angle due to which they end up further from the axis at the retarding electrode. At this transverse position further off-axis the voltage changes faster with the transverse position. This results in a lower resolution of the RFA due to the finite size of the beam.

The offsets of the ionization position with respect to the axis in the simulations in figure 8 are not unrealistic given the accuracy of the accelerator translation. Furthermore, misalignments of the individual electrodes in the accelerator and RFA can also be of the same order. Therefore it is concluded that such misalignments are likely the cause of the more than linear growth of energy spread with the extraction field. Regardless of the simulations, the measured data presented in figure 8 gives an upper bound for the energy spread of the created ion beam for various E .

F. Beam current

The measurements shown before this section were all performed on a beam which was selected with a selection aperture with a diameter of $21 \mu\text{m}$. In this way a beam was created with a current of roughly 9 pA . When selecting the atomic beam with a larger aperture more current can be created. Figure 9 shows the energy distribution for a current of 280 pA , which was created by using a

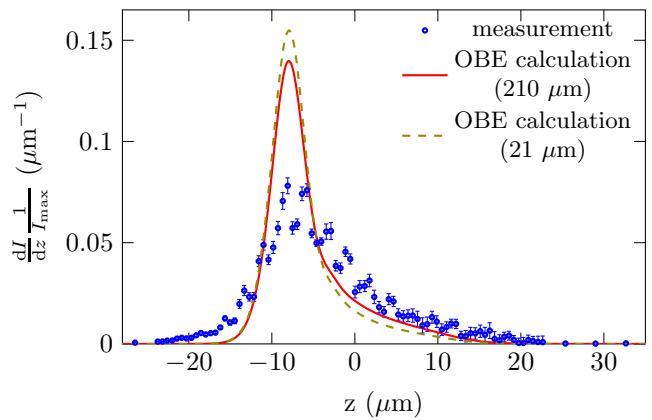


FIG. 9. Measured (markers with error bars indicating the standard deviation) and calculated (lines) ionization position distribution for a current of 280 pA . The experiment was performed with $I_i = 1.3 \times 10^{10} \text{ W/m}^2$, $s = 1.3 \times 10^2$, $E = 37 \text{ kV/m}$, $U = 1 \text{ keV}$, $V_f = 850 \text{ V}$ and $d = 210 \mu\text{m}$.

selection aperture with a diameter of $210 \mu\text{m}$. Note that this diameter is significantly larger than the $1/e^2$ diameter of the ionization laser beam of $68 \mu\text{m}$. This means that atoms at a different y -position (for orientation reference see figure 1) will experience a different ionization intensity that ranges from I_i at $y = 0$ to almost zero at the edges. These atoms at the edge will thus ionize over a larger range which increases the energy spread in the beam. As can be seen from the calculated curves in figure 9 this is indeed the case. The calculated ionization position distribution for a beam selected with a $210 \mu\text{m}$ aperture (solid curve) is indeed slightly broader than the distribution calculated for a selection aperture of $21 \mu\text{m}$ (dashed curve). However, the measured distribution is broader than both of these curves as well as the measured distribution at a lower current under the same circumstances (see fourth panel in figure 7a). A reason for this broadening can be the resolution of the RFA, especially because the beam is now approximately 3 times larger in the x -direction. In the y -direction the beam is also larger, although less due to the limited size of the ionization laser beam waist [12]. Due to this larger size the beam will probe a larger range of voltages in the aperture of the retarding electrode. However, note that the measured full width 50% energy spread of the beam with a current of 280 pA is still only $(0.311 \pm 0.005) \text{ eV}$.

G. Beam energy

The advantage of the two stage acceleration in the AB-LIS setup is that a beam with a different energy can be created while maintaining the same extraction field at the position of ionization. In this way the energy spread of the beam is independent of the beam energy. The measurements shown before this section were all performed on a beam with an energy of 1 keV . Figure 10 shows the measured (circular markers with error bars) energy

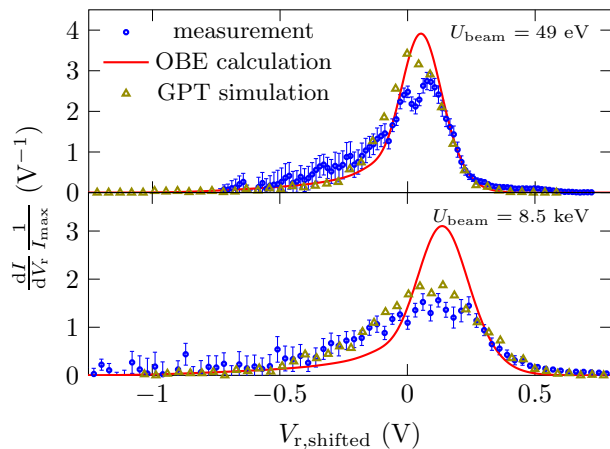


FIG. 10. Measured (markers with error bars indicating the standard deviation) and calculated (lines) ion energy distribution for ions with an energy of 49 eV (top) and 8.5 keV (bottom). The triangular markers show the result of a particle tracing simulation in which the expected distribution of energies is analyzed with the retarding field analyzer, thus including finite resolution effects. The experiments are performed with $I_i = 1.9 \times 10^{10}$ W/m², $s = 1.3 \times 10^2$, and $d = 21$ μ m. In the case of $U = 49$ eV, $E = 41$ kV/m and $V_f = 42$ V. In the case of $U = 8.5$ keV, $E = 51$ kV/m and $V_f = 7375$ V.

distributions for a beam with an energy of only 49 eV (top panel) and a beam with an energy of 8.5 keV (bottom panel). Shown are also the expected distributions from the optical Bloch equation calculation (lines) and simulation results in which the RFA was used to extract the energy distribution of the beam (triangular markers). Note that the measurements at $U = 8.5$ keV are performed with a slightly higher extraction field of 51 kV/m as compared to 41 kV/m for the measurement at $U = 49$ eV.

The measured, calculated and simulated energy distributions at $U = 49$ eV all agree well with each other. The measured distribution is slightly broader than the other two, mostly visible by the slightly longer tail on the low energy side and the higher peak value. The full width 50% energy spread of the measured distribution amounts (0.215 ± 0.005) eV. The measured distribution at 8.5 keV differs more from its expected distribution. However, the simulated distribution which includes finite resolution effects, does agree well with the measurement. They differ from the calculated distribution because the RFA resolution becomes lower for increasing beam voltage, since the retarding voltage distribution over the cross section

of the aperture in the retarding electrode scales with the beam energy. The full width 50% energy spread of the measured distribution amounts (0.38 ± 0.02) eV. These experiments, together with simulations, show that the energy spread of the beam is independent of the energy itself and is only determined by the extraction field in which the ions are created and the ionization position distribution.

V. CONCLUSION

The energy distribution of an ultracold ion beam is measured using a retarding field analyzer (RFA). The energy distribution is measured for different excitation and ionization laser intensities. In general, the distributions show a large degree of similarity with expected distributions found by numerically solving the optical Bloch equations under conditions similar as in the experiment [12]. The differences that are present can be explained by a possibly different excitation laser beam shape in the experiment than in the calculation.

As the ions in the ABLIS setup are accelerated in two steps, it is possible to set the extraction field independent of the beam energy. Therefore the energy spread is independent of the beam energy, which was verified experimentally at 49 eV and 8.5 keV. The energy distribution is completely determined by the ionization position distribution, influenced by the excitation and ionization laser beam intensities, and the extraction electric field. The measured energy spread increased more than linear with the extraction field. Simulations show that this is likely caused by ions being created off-axis in the accelerator, which lowers the resolution of the RFA.

The smallest full width 50% ionization position distribution width measured is (5.6 ± 0.2) μ m. With an extraction field of 37 kV/m this gives rise to an energy spread of (0.205 ± 0.006) eV. With the experimentally reached beam density taken into account, this electric field would be large enough to create a pencil beam containing a current of 3 pA, thus preventing disorder-induced heating [13].

ACKNOWLEDGMENTS

This work is part of the research programme Ultracold FIB with project number 12199, which is (partly) financed by the applied and engineering sciences division of the Netherlands Organisation for Scientific Research (NWO). The research is also supported by Thermo Fisher Scientific, Pulsar Physics and Coherent Inc.

-
- [1] Joachim Mayer, Lucille A. Giannuzzi, Takeo Kamino, and Joseph Michael, TEM Sample Preparation and FIB-Induced Damage, MRS Bull. **32**, 400–407 (2007).
 [2] D.M. Donnet and H. Roberts, FIB applications for semi-

conductor device failure analysis, in *Microsc. Semicond. Mater. Springer Proc. Phys.*, edited by A.G. Cullis and J.L. Hutchison (Springer, Berlin, Heidelberg, 2005) pp. 403–408.

- [3] Richard H Livengood, Paul Winer, and Valluri R Rao, Application of advanced micromachining techniques for the characterization and debug of high performance microprocessors, *J. Vac. Sci. Technol. B* **17**, 40 (1999).
- [4] L. W. Swanson, G. A. Schwind, and A. E. Bell, Measurement of the energy distribution of a gallium liquid metal ion source, *J. Appl. Phys.* **51**, 3453–3455 (1980).
- [5] Miroslav Kolíbal, Tomáš Matlocha, Tomáš Vystavěl, and Tomáš Šíkola, Low energy focused ion beam milling of silicon and germanium nanostructures, *Nanotechnology* **22**, 105304 (2011).
- [6] J. J. McClelland, A. V. Steele, B. Knuffman, K. A. Twedt, A. Schwarzkopf, and T. M. Wilson, Bright focused ion beam sources based on laser-cooled atoms, *Appl. Phys. Rev.* **3**, 011302 (2016).
- [7] A V Steele, A Schwarzkopf, J J McClelland, and B Knuffman, High-brightness Cs focused ion beam from a cold-atomic-beam ion source, *Nano Futur.* **1**, 015005 (2017).
- [8] B Knuffman, A V Steele, and J J McClelland, Cold atomic beam ion source for focused ion beam applications, *J. Appl. Phys.* **114**, 44303 (2013).
- [9] L. Kime, A. Fioretti, Y. Bruneau, N. Porfido, F. Fuso, M. Viteau, G. Khalili, N. Santic, A. Gloter, B. Rasser, P. Sudraud, P. Pillet, and D. Comparat, High-flux monochromatic ion and electron beams based on laser-cooled atoms, *Phys. Rev. A* **88**, 033424 (2013).
- [10] S. H. W. Wouters, G. ten Haaf, R. P. M. J. W. Notermans, N. Debernardi, P. H. A. Mutsaers, O. J. Luiten, and E. J. D. Vredenburg, Performance predictions for a laser-intensified thermal beam for use in high-resolution focused-ion-beam instruments, *Phys. Rev. A* **90**, 063817 (2014).
- [11] G. ten Haaf, T. C. H. de Raadt, G. P. Offermans, J. F. M. van Rens, P. H. A. Mutsaers, E. J. D. Vredenburg, and S. H. W. Wouters, Direct Magneto-Optical Compression of an Effusive Atomic Beam for Application in a High-Resolution Focused Ion Beam, *Phys. Rev. Appl.* **7**, 054013 (2017).
- [12] G. ten Haaf, S. H. W. Wouters, P. H. A. Mutsaers, and E. J. D. Vredenburg, Cavity-enhanced photoionization of an ultracold rubidium beam for application in focused ion beams, accepted for publication in *Phys. Rev. A* (2017), arXiv:1708.01933 [physics.atom-ph].
- [13] G. ten Haaf, S. H. W. Wouters, S. B. van der Geer, E. J. D. Vredenburg, and P. H. A. Mutsaers, Performance predictions of a focused ion beam from a laser cooled and compressed atomic beam, *J. Appl. Phys.* **116**, 244301 (2014).
- [14] J. Arol Simpson, Design of retarding field energy analyzers, *Rev. Sci. Instrum.* **32**, 1283–1293 (1961).
- [15] See <http://www.pulsar.nl/gpt> for General Particle Tracer Code by Pulsar Physics,.
- [16] See <https://www.cst.com/products/cstems> for Computer Simulation Technology EM Studio software,.
- [17] R. R. Freeman and N. P. Economou, Electric field dependence of the photoionization cross section of Rb, *Phys. Rev. A* **20**, 2356 (1979).
- [18] David A. Harmin, Theory of the Stark effect, *Phys. Rev. A* **26**, 2656 (1982).